SAND2022-1373C

22PFL-0220

Non-Equilibrium Law-of-the-wall Modeling for Improved Heat Transfer Predictions: Model Development and Validation

Author, co-author (Do NOT enter this information. It will be pulled from participant tab in MyTechZone)

Affiliation (Do NOT enter this information. It will be pulled from participant tab in MyTechZone)

Abstract

A one-dimensional, non-equilibrium, compressible law of the wall model is proposed to increase the accuracy of heat transfer predictions from computational fluid dynamics (CFD) simulations of internal combustion engine flows on engineering grids. Our 1D model solves the transient turbulent Navier-Stokes equations for mass, momentum, energy and turbulence under the thin-layer assumption, using a finite-difference spatial scheme and a high-order implicit time integration method. A new algebraic eddy-viscosity closure, derived from the Han-Reitz equilibrium law of the wall, with enhanced Prandtl number sensitivity and compressibility effects, was developed for optimal performance. Several eddy viscosity sub-models were tested for turbulence closure, including the two-equation k-epsilon and k-omega, which gave insufficient performance. Validation against pulsating channel flow experiments highlighted the superior capability of the 1D model to capture transient near-wall velocity and temperature profiles, and the need to appropriately model the eddy viscosity using a low-Reynolds method, which could not be achieved with the standard two-equation models. The results indicate that the non-equilibrium model can capture the near-wall velocity profile dynamics (including velocity profile inversion) while equilibrium models cannot, and simultaneously reduce heat flux prediction errors by up to one order of magnitude. The proposed optimal configuration reduced heat flux error for the pulsating channel flow case from 18.4% (Launder-Spalding law of the wall) down to 1.67%.

Introduction

With carbon dioxide emissions now being a major source of environmental concern from combustion devices, and engine efficiency improvements being of the order of a few percentage points, efforts to improve multidimensional simulations have recently shifted towards a focus on near-wall phenomena [1]. In diesel engine modeling, spray-wall interactions have historically played a more important role over wall-heat transfer: high-temperature flames do not reach the walls often, and when they do, they hit the piston surface. Focus has been to engineer a piston geometry that promotes in-cylinder air utilization, to increase combustion efficiency and reduce engine-out soot and NOx emissions [2, 3]. Yet, equilibrium wall models are still largely adopted in most engineering simulations, but pose significant modeling challenges, because they involve strong simplifying assumptions – most notably: equilibrium itself – that drastically reduce their physics content [4]. Figure 1 represents the predicted heat transfer from the cylinder walls of the Sandia heavy-duty engine platform under motored conditions, from [5], employing a Reynolds-Averaged Navier-Stokes (RANS) turbulence model and different equilibrium law-of-the-wall models.

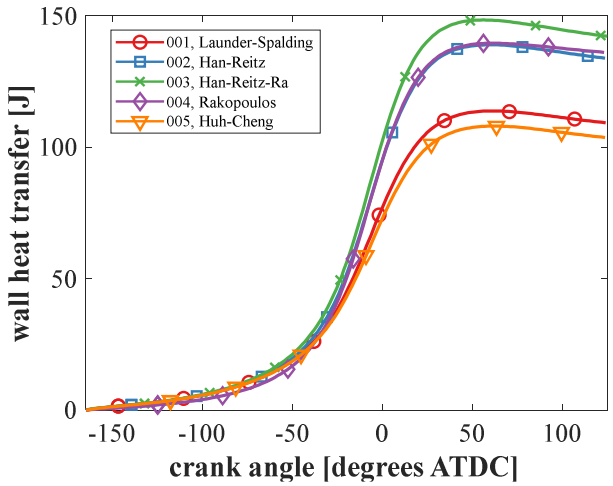

Figure 1. Predicted wall heat transfer from the cylinder in the Sandia heavy duty engine under motored conditions, with several equilibrium wall models.

Despite no combustion and a low-swirl chamber configuration, deviations of more than 40% are observed based on the model choice.

Because temperature timescales are much longer in the metal than on the fluid side, wall phenomena in engine computational fluid dynamics (CFD) simulations are commonly patched as boundary conditions to the CFD solver as part of the operator splitting approach [6]. Near-wall momentum and temperature fields are modeled following different approaches, as summarized in Figure 2 and below:

a. The first approach employs the "High-Reynolds number" assumption, typical of RANS simulations. It is assumed that the size of the first cell layer near the wall is large enough to contain the whole boundary layer's viscous sub-layer, such that the fluid-side nodes are located well into the developed log-law part of the velocity profile, at non-dimensional locations $y^+ \geq 100$. Velocity and temperature profiles are modeled. Their effect on finite-volume conservation closures comes from formulas, which represent analytical integrals of simple versions of the momentum and energy

conservation equations in the 1D domain. Wall functions of temperature have been proposed over the decades (e.g.: [7, 8, 9]) to account for different simplifying assumptions. Because all quantities are modeled, this is the approach that yields the largest mesh dependency.

b. The "Low-Reynolds number" assumption, common to Large Eddy Simulations (LES) and Detached Eddy Simulation (DES), assumes that the grid discretization near the wall is both well-behaved – with layers well-aligned in the wall-normal direction where the gradients are – and fine enough that the first cell layer near the wall is within the viscous sub-layer, i.e., $y^+ \leq 1$. In DES, a different turbulence model, i.e. from RANS, is solved in the near-wall region. This reduces the impact of all the simplifying assumptions in the law-of-the-wall formulation, most notably that of equilibrium. But, it comes at the price of significantly larger computational cost and introduces mesh dependency.

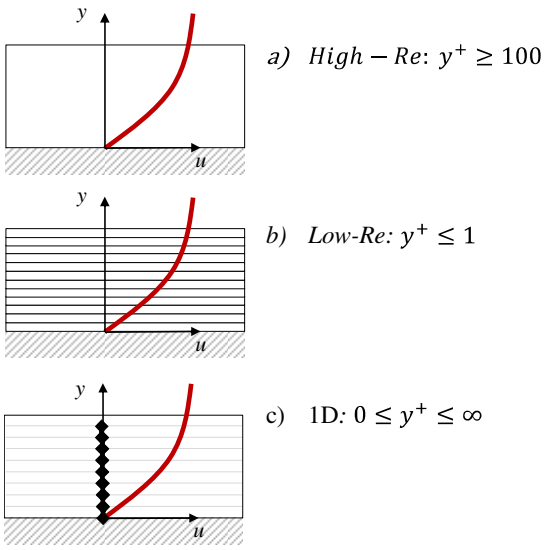

Figure 2. Near-wall flow treatment modes. *a)* High-Re, equilibrium law of the wall; *b)* Low-Re, wall-resolved mesh; *c)* (this work) 1D non-equilibrium wall model.

c. Non-Equilibrium wall models. A third class of models provides high-resolution alternatives to wall functions by embedding a further discretization between the last fluid layer and the wall – the most notable example being Wall-Modeled LES (WMLES) [4]. These models do not have special requirements as far as the mesh is concerned, since they only match the main CFD grid via the fluid-side boundary conditions. They can solve arbitrary sets of equations, as wall heat flux and shear friction coefficients, which are then passed back to the CFD solver like any other wall function.

Such a modeling approach was recently brought to the engine field by Ma et al. [10], who demonstrated that such high-fidelity is appropriate for internal combustion engine boundary layers. In the same way, we present a new non-equilibrium wall model of this latter class, whose purpose is to enhance wall heat transfer predictions in both RANS and LES of internal combustion engines. The major contributions of this paper are summarized as follows:

- We validated our model against simultaneous velocity and temperature profiles of a well-characterized set of pulsating channel flow experiments;
- We found that non-dimensional boundary layer scaling plays a very important role in high-temperature, compressible conditions, and propose a suitable formulation for it;
- We tested both algebraic and two-equation eddy viscosity closures, and found that two-equation turbulence models do not justify the additional computational cost, as they only work well in their "low-Reynolds" formulations, i.e., when a near-wall algebraic formula is also patched to them;
- Focusing on heat transfer rather than on velocity profile predictions, we found that temperature is far more sensitive to the turbulence closure than momentum. So, we propose an "enhanced Han-Reitz" eddy viscosity closure, which responds to both laminar and turbulent Prandtl number variations and to accurate molecular transport properties;
- With compressible scaling and accurate algebraic eddy viscosity, the non-equilibrium wall boundary model reduced predicted wall heat flux errors by more than one order of magnitude compared to equilibrium laws-of-the-wall.

Non-Equilibrium Wall Model

The set of governing equations for the one-dimensional domain with the compressible thin-layer assumption ($\partial_x = 0$) can be written as:

Continuity:

$$\partial_t \rho + \mathbf{u} \cdot \nabla \rho = 0, \quad (1)$$

(with density ρ, velocity vector $\mathbf{u}$) includes closure in the wall-normal direction.

Energy:

$$\partial_t h + \boldsymbol{u} \cdot \nabla h = \nabla \cdot \left[\left(\frac{\mu}{Pr} + \frac{\mu_t}{Pr_t}\right)\nabla T\right] + A_0 \rho \epsilon + \mu_t (1 - A_0)\sigma_{ij} : \nabla \boldsymbol{u}, \quad (2)$$

employs the eddy-viscosity (μ_t) model for the turbulent diffusion term, and dissipation is sourced from either the viscous flow tensor (flag $A_0 = 0$) or the turbulence kinetic energy dissipation ϵ if a two-equation turbulence closure is used ($A_0 = 1$).

Momentum:

$$\partial_t(\rho \boldsymbol{u}) + \boldsymbol{u} \cdot \nabla(\rho \boldsymbol{u}) = -\frac{\nabla p}{a^2} + \nabla \cdot \mu_t \left[\nabla \boldsymbol{u} + \nabla \boldsymbol{u}^T - \tfrac{2}{3}\delta_{ij}(\nabla \cdot \boldsymbol{u})\right], \quad (3)$$

includes the wall-normal pressure gradient term with the Amsden's scaling (a) method [11] to improve numerical convergence of the implicit iterations.

Eddy viscosity closure. Turbulence equations are employed when a two-equation closure for the eddy viscosity term, e.g. k-epsilon model, is used [12]. They are:

$$\partial_t \rho k + \nabla \cdot (\rho \boldsymbol{u} k) = \nabla \cdot \left(\frac{\mu_t}{Pr_k}\nabla k\right) - \rho(\epsilon + D) - \frac{2}{3}\rho k(\nabla \cdot \boldsymbol{u}) + \mu_t \sigma_{ij} : \nabla \boldsymbol{u}, \quad (4)$$

$$\partial_t \rho \epsilon + \nabla \cdot (\rho \boldsymbol{u} \epsilon) = \nabla \cdot \left(\frac{\mu_t}{Pr_\epsilon}\nabla \epsilon\right) + \rho \frac{\epsilon}{k}(C_{\epsilon 1} P - C_{\epsilon 2}\epsilon) - \rho R + C_3 \rho \epsilon (\nabla \cdot \boldsymbol{u}). \quad (5)$$

Four two-equation models were tested overall: RNG k-epsilon model [13] (with the fixed implementation reported in [14]); 1974 low-Reynolds k-epsilon model [7]; 2019 low-Reynolds k-epsilon model [15]; 2006 k-omega model [16]. Three algebraic eddy viscosity closures were also formulated:

Constant eddy viscosity:

$$\mu_t = \mu_0, \tag{6}$$

Mixing-Length closure [17]:

$$\mu_t = \rho \frac{\partial u}{\partial y}\Big|_w \left(\kappa y \cdot \left(1 - e^{-y^+/A^+}\right)\right)^2, \tag{7}$$

Han-Reitz closure [8], as employed in the well-established temperature wall function:

$$\mu_t = \mu \cdot Pr_t \cdot \begin{cases} (a + by^+ + cy^{+2}) & y^+ \le 40 \\ m \cdot y^+ & y^+ > 40 \end{cases} \tag{8}$$

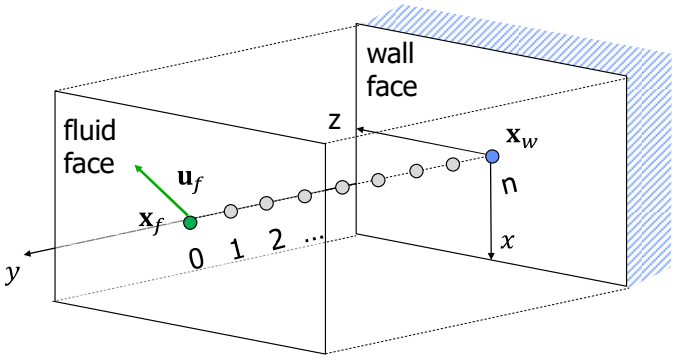

Figure 3. Schematic of the finite-difference boundary layer discretization.

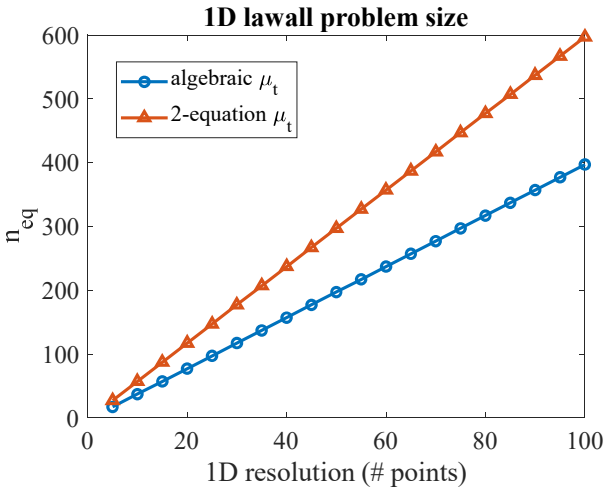

Figure 4. Computational complexity of the finite-difference problem.

Numerical Setup

The conservation equations are solved in a variable-size finite difference framework with a bi-geometric node distribution for improved accuracy near the boundaries.

Homogeneous, zero-gradient boundary conditions (BCs) are applied in the far-field, and no-slip conditions at the wall, as represented in Figure 3. We use a staggered grid approach that stores extensive (volumetric) fields at the cell centroids and the momentum field at the nodes. The time derivatives of the conservation equations are wrapped into an array of Ordinary Differential Equations (ODEs), which is solved with the implicit Backward Differentiation Formulas (BDF) [18]. As shown in Figure 4, employing a two-equation turbulence model significantly increases the problem size, as 6 equations are to be solved instead of 4. The sparsity pattern of the Jacobian matrix is characterized by a finite-difference block-tridiagonal structure for each variable. The expected computational cost of its solution in each near-wall cell of a CFD solver is hence expected to be similar to that of a sparse chemistry system of the same size [19].

Basic Validation

Stokes oscillating flow**.** To validate the numerical framework, we tested well-established problems where an analytical solution was available. The first was with Stokes oscillating flow. This problem has a pulsating far-field velocity and a no-slip boundary condition at the wall, with a constant viscosity term, and solution:

$$u(y,t) = U_\infty(cos(\omega t) - exp(\phi)\, cos(\omega t + \phi)), \tag{9}$$

with $\phi = -y\sqrt{\omega/2\nu}$. As there is no advection, this is a good test for the momentum diffusion operator. Figure 5 reports a comparison between predicted and analytical solutions for a case with engine-like conditions: $\omega = 2000rpm$, $\nu = 0.0015cm/s^2$, $U_\infty = 100cm/s$. High fidelity was retained even after several cycles were simulated.

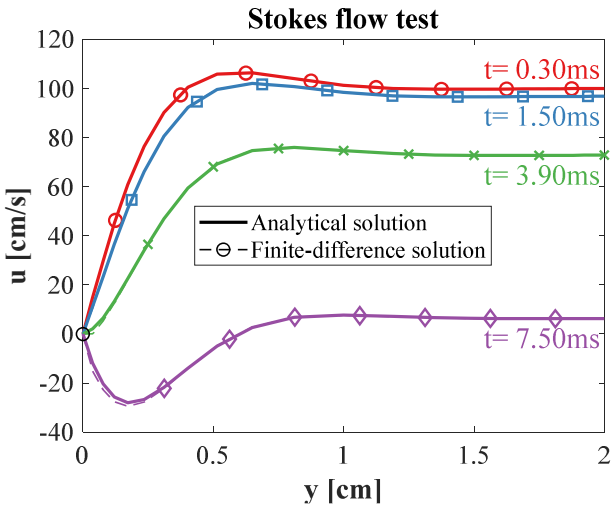

Figure 5. Stokes oscillating flow problem: analytical (solid lines) vs. simulated (dashed lines + marks) solutions at select times.

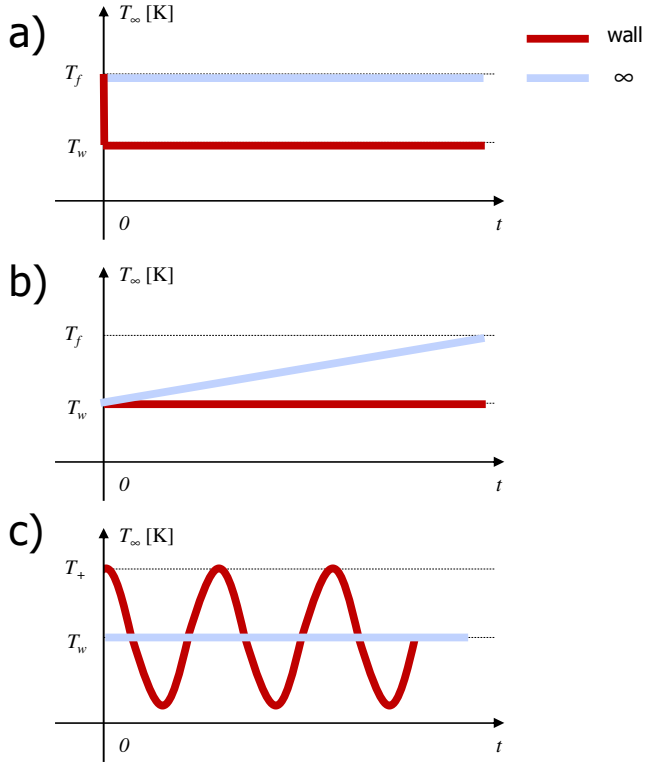

Figure 6. Boundary temperature signals for the analytical heat transfer equation. a) Step-wise change; b) linear change; c) pulsating temperature.

Heat equation. Three analytical solutions to the transient 1D heat conduction equation [19] were used to test the accuracy of the energy equation. These cases have a homogeneous far-field BC and a time-varying wall boundary temperature, subject to different signals, as reported in Figure 6: a) step-wise temperature change; b) linear change; c) pulsating change. The heat conduction diffusion coefficient $\alpha = \mu_t/(\rho Pr_t)$ was assumed from $\mu_t = 0.0002 g/cm \cdot s$ and the density of nitrogen at 1 atmosphere, with far-field $T_f = 1180K$ and base wall temperature $T_w = 500K$.

With the step-wise temperature change (Figure 7), the finite-difference solver predicted the diffusion-driven erf solution well even after some time, when it tends towards a zero-diffusion (i.e., linear) temperature profile. With the linear temperature change (Figure 8) the transient profile was still well-matched, and both the zero-gradient and the wall-temperature BCs showed accurate behavior. With the pulsating case of Figure 9, again, good accuracy was observed, even though the central part of the domain (y between 0.2 and 0.3 cm) exhibited some slight offset due to numerical error.

The third validation case is a good example of why capturing transient features is important in non-equilibrium flows: at 90 and 270 degrees, the wall and fluid-side temperatures are the same. Any equilibrium law of the wall would predict zero heat transfer here. Instead, the transient 1D predictions show that *dT/dy* is at near-peak values in both these cases, and even more relevantly, with opposite signs. No equilibrium models could ever capture any of this behavior.

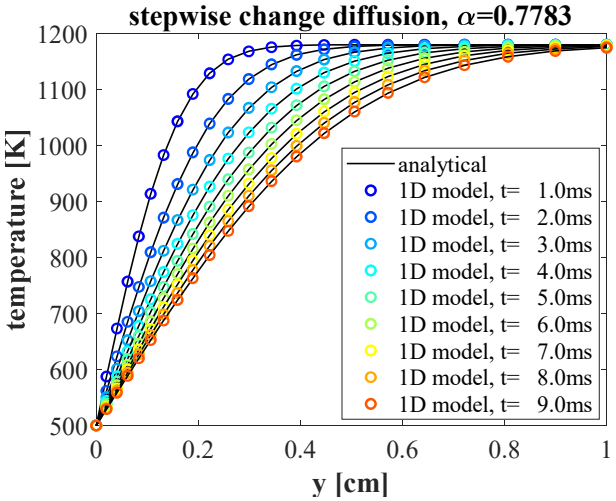

Figure 7. Predicted vs. analytical solution for the step-wise temperature change heat conduction equation.

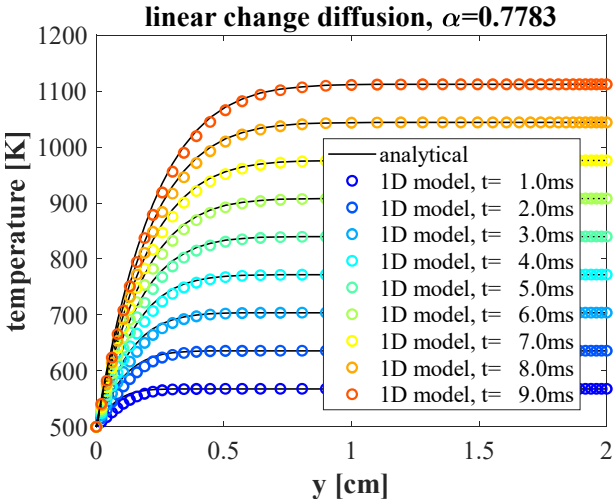

Figure 8. Predicted vs. analytical solution for the linear temperature change heat conduction equation.

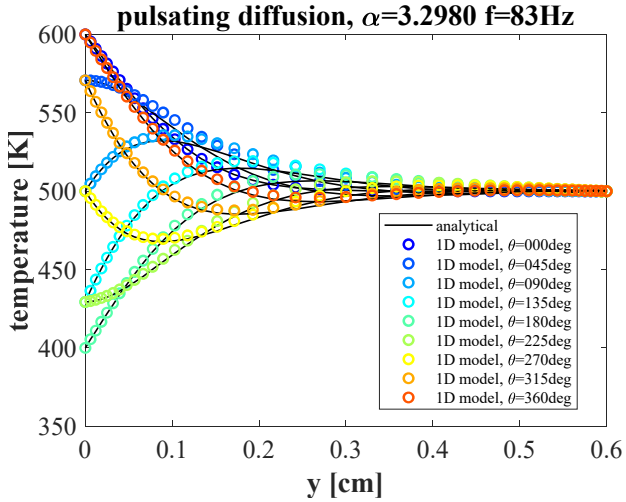

Figure 9. Predicted vs. analytical solution for the oscillating temperature change heat conduction equation.

Hot Pulsating Channel Flow

Study of model parameters and the eddy viscosity closure was carried out against the experimental measurements of Dec et al. [20, 21]. This unique set of experiments feature a pulsating combustor as represented in the schematic of Figure 10. The pulse combustor is fed with stoichiometric methane-air mixtures and is connected to a long, glass tailpipe with fixed diameter D=30mm. Exhaust gases flow is subjected to the combustor's oscillations, and the tailpipe length could be adjusted to achieve different frequencies. The same combustor conditions were probed for both velocity with Laser-Doppler Velocimetry (LDV) and temperature with the Two-Line Atomic Fluorescence (TLAF) method. The relatively-low base combustion frequency (f=83 Hz) allowed the authors to extract both ensemble-averaged and turbulence fluctuation signals out of the time-resolved measurements of velocity and temperature. Instantaneous heat flux measurements were also acquired by means of a high-speed thin-wire thermocouple.

This set of experiments provided a unique opportunity for the simultaneous validation of temperature and momentum boundary layers, thanks to:

- Fully turbulent conditions (Re~3750);
- Simultaneous velocity and temperature measurements;
- Time-resolved turbulence boundary conditions at the centerline;
- Heat flux data is performed with a separate device and not derived from dT/dy at the wall.

To model these conditions, the non-equilibrium 1D model was run standalone, i.e., it was used to model the whole half-pipe, and not just as a near-wall cell BC. At times of peak velocity, the flow condition at the centerline reached $y^+ > 450$, i.e., characterizing a fully-developed log-law velocity profile.

Compressible boundary layer scaling

To model this large boundary layer, non-dimensional scaling of the boundary layer coordinate, which is incompressible, had to be improved:

$$y_w^+ = \frac{\rho_w u_\tau y}{\mu_w}, \tag{10}$$

the normalized distance from the wall, is scaled using wall values of density and molecular viscosity. However, with the experiment temperatures ranging between 500K at the wall and ~1200K at the centerline, density changes by ~2.4x, and viscosity by ~$\sqrt{2.4}$x. So, the choice of the density and viscosity values in Equation 10 becomes relevant. As research in compressible WMLES also suggested, four different compressible formulations were tested as summarized in [22]. Among them, the "semi-local" formulation was found to provide the best accuracy:

$$y_{sl}^+(y) = \frac{\sqrt{\rho_w \rho(y)} u_\tau y}{\mu(y)}. \tag{11}$$

Density in this formulation is the geometric average between the wall and the current location, and the local molecular viscosity level is used. The comparison of Figure 11 shows that the incompressible scaling (Eqn. *10*) *underestimates* the boundary layer thickness and *overestimates* $y+$, due to the (highest) density at the wall not being representative of most of the fluid core. That ultimately leads to overestimating the wall friction velocity and its dissipation.

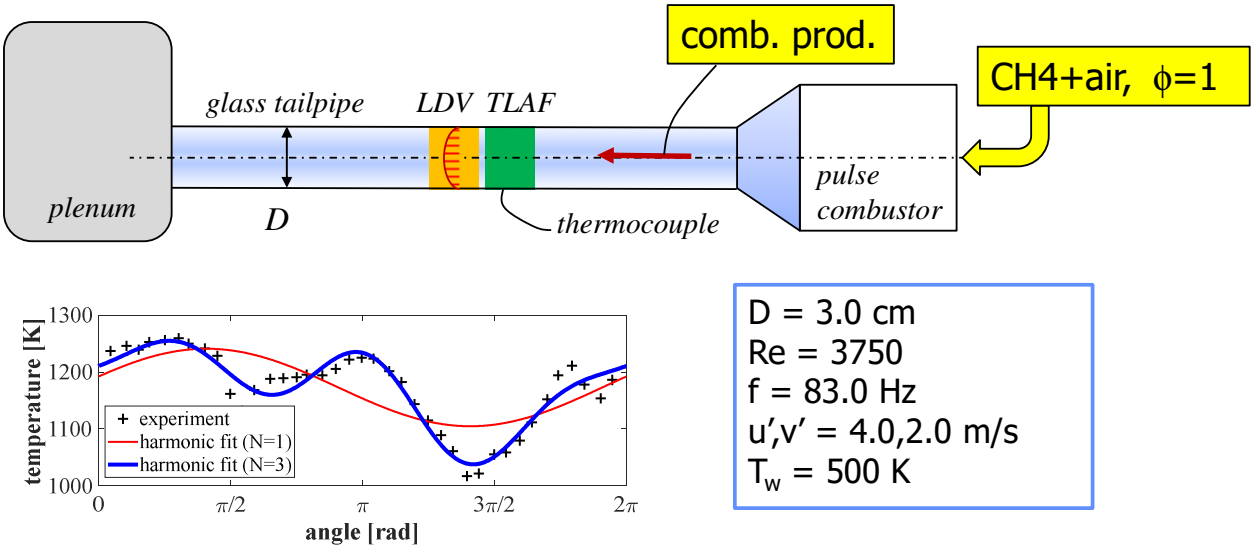

Figure 10. Schematic representing the pulsating combustor configuration of Dec et al. [21], as well as the centerline temperature BC filtering.

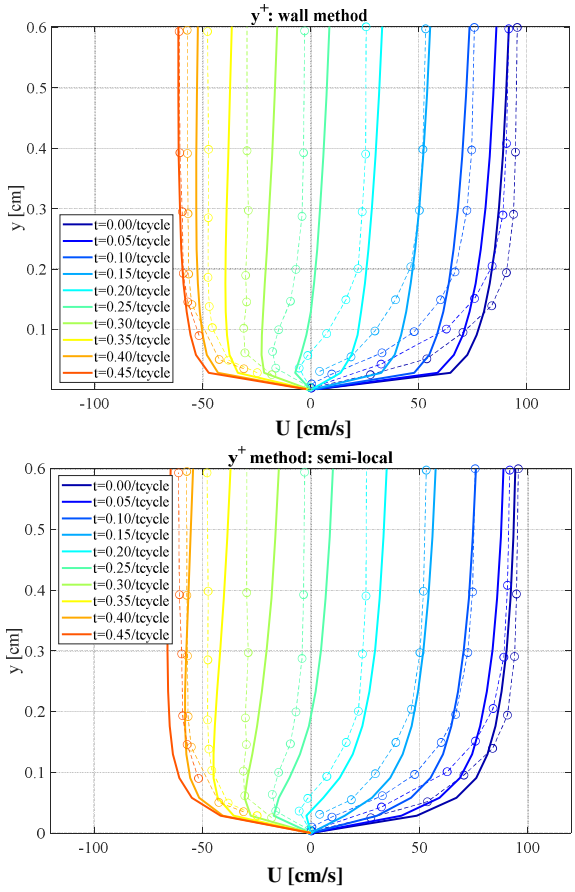

Figure 11. Time-resolved velocity profiles with two formulations for boundary-layer scaling y+: (top) incompressible; (bottom) compressible "semi-local" formulation. Han-Reitz eddy viscosity model. Dotted lines with circle markers are measured values; solid lines are from the simulations.

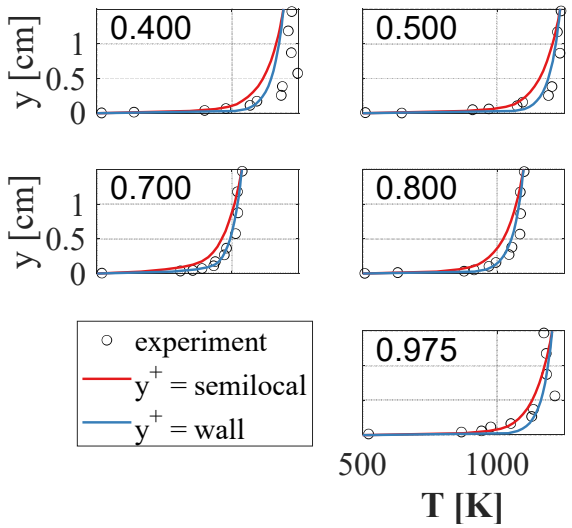

Figure 12. Temperature profiles at some normalized times t/period=0.4, 0.5, 0.7, 0.8, 0.975, as indicated in the top-left corner of each plot, with different y+ formulations and the Han-Reitz eddy viscosity model: incompressible "wall"; compressible or "semilocal".

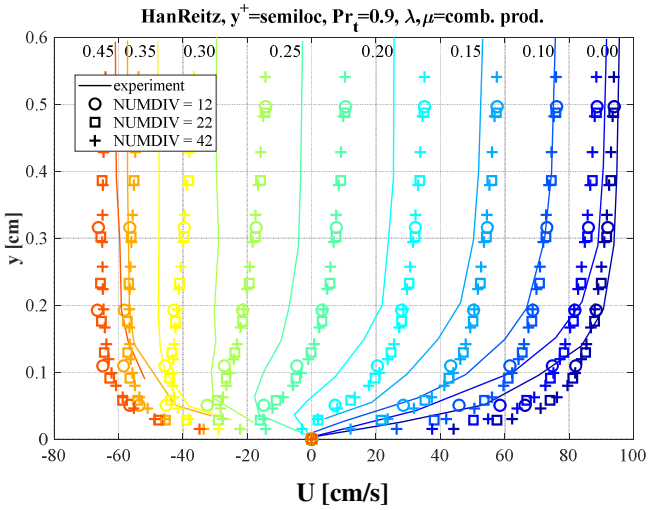

Figure 13. Solution dependency on the number of 1D points.

Figure 12 shows the corresponding temperature predictions at five snapshots through the oscillation period. Even with proper momentum BL scaling, none of the approaches captured the steep near-wall temperature gradients well, and the compressible $y+$ formulation showed even worse predictions than the original incompressible Han-Reitz model. Because the Han-Reitz model was developed for temperature only, its turbulent Prandtl number was hardcoded into the model (Pr_t=0.72 [8]); Figure 13 indicates that a successful transient model will require that the two boundary layer sizes be decoupled through the use of a variable Pr_t as described below.

1D Mesh Dependency. To rule out numerical discretization as a potential source of inaccuracy, a mesh dependency study was run, as reported in Figure 13. The same problem was simulated with either N=12, 22, or 42 points, corresponding to average cell sizes $\Delta y \approx 1.4, 0.7, 0.37mm$, and peak $y+$ ranges $\Delta y^+ \sim 41, 21, 11$, respectively.

All solutions yielded essentially identical results, most notably for the temperature profiles (not shown because they are completely overlapping), and with negligible discrepancies within the predicted velocities.

This was an important finding, as it proved that the model is capable of nearly mesh-independent results even when the $y+$-per-cell range is large, which is necessary when the model is coupled as a near-wall layer in engineering-size grids, and to keep the total simulation time under control.

Eddy viscosity model analysis

Constant viscosity. The compressibility analysis showed that (with Han-Reitz closure) very good instantaneous velocity predictions could be achieved, but not so much for temperatures. Since momentum (Eqn. 3) and energy (Eqn. 2) involve the same eddy viscosity, more efforts were devoted to understand its non-trivial role in the relationship between the velocity and temperature profiles.

First, a constant eddy viscosity model was used (Equation 6). It was found that very good accuracy could be achieved modeling either, but not simultaneously, the velocity or the temperature profiles, by simply adjusting μ_0.

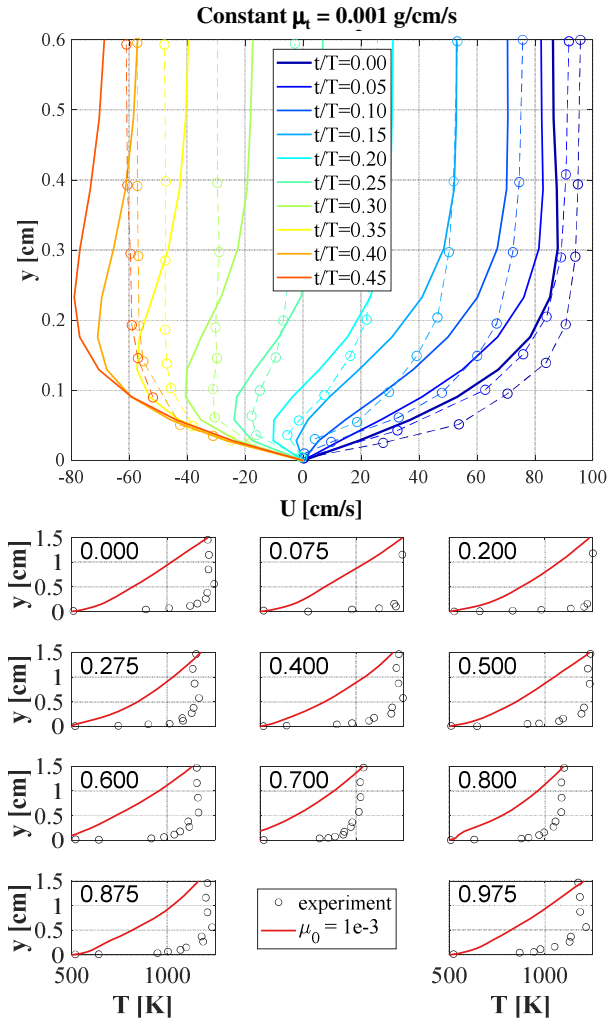

Figure 14. Predicted velocity and temperature profiles with constant eddy viscosity, $\mu_0 = 1e-3[g/cm \cdot s]$.

For example, constant $\mu_0 = 0.001 g/cm/s$ achieves good velocity predictions. However, great temperature errors are again seen in this case.

Two-equation turbulence models. Two-equation turbulence models have been suggested as appropriate closures for this class of problems [10]. A summary of the results from four different formulations is reported in Figure 15:

- The standard k-epsilon model has long been known to have large errors in near-wall flows (see, for example, [23] or [14]). Similar behavior was seen in the 1D boundary layer model, with greatly over-predicted eddy viscosity to the extent that all temperature and velocity gradients were heavily smeared;
- While the k-omega is supposed to yield better behavior near the walls than k-epsilon [16] it performed similarly poorly;
- When near-wall damping is present, the k-epsilon model can produce decently accurate results of both velocity and temperature profiles; in particular, the 2019 formulation of [15] produced good results. This formulation features a near-wall damping function, which is valid at any distance from the wall, is a function of k, epsilon, and the local rate of strain, and has been validated against DNS data.

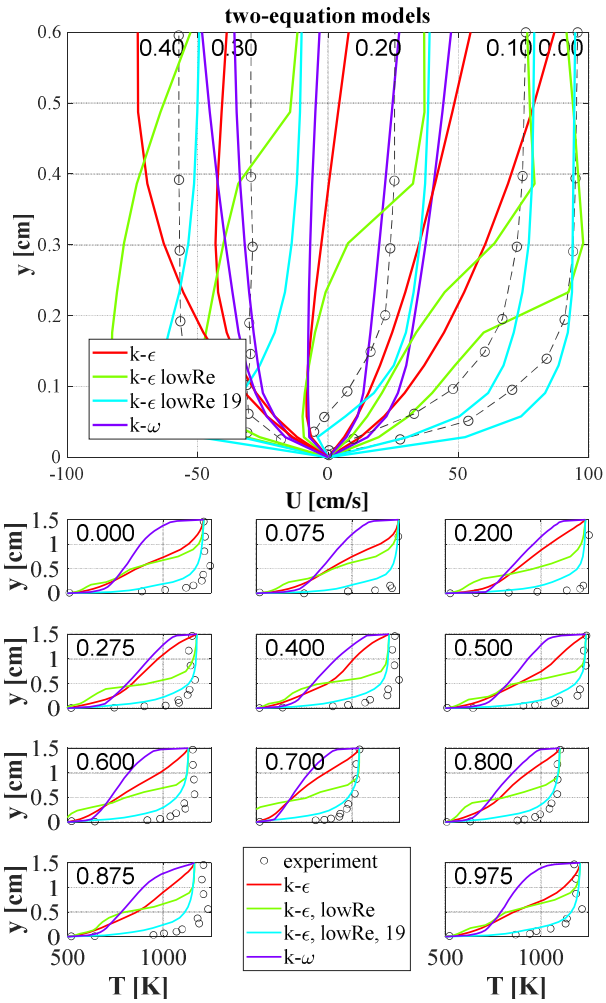

Figure 15. Predicted velocity and temperature profiles with different turbulence models at select normalized times during the period. Dashed lines with circle markers are measured values; solid lines are the simulation results.

Because near-wall damping functions are a way to superimpose an algebraic eddy viscosity near the walls on top of a turbulence model, attention was focused on plain algebraic eddy viscosity models and their model parameters.

Algebraic eddy viscosity models. Two algebraic models using the mixing length concept (Eqn. *7*) and the Han-Reitz model (Eqn. *8*) are shown in Figure 16. Both models exhibit better results compared to most of the two-equation turbulence models, and the Han-Reitz model clearly exhibits the best trade-off in capturing both momentum and the temperature boundary layers with appropriate accuracy. In fact, the mixing-length concept, while generally good at capturing velocities, strongly underestimates the temperature boundary layer thickness. This would likely lead to a severe over-estimation of the wall heat transfer rates.

Variable-Prandtl algebraic eddy viscosity

The algebraic Han-Reitz model was further analyzed considering its good performance 'out of the box', and an improved version to it is proposed in this work. In the original work by Han and Reitz [8], the eddy viscosity term was needed in analytical form, because it had to be embedded and integrated in the wall heat flux analytical integral.

Han and Reitz achieved this closure by equating two different formulations for the non-dimensional eddy viscosity:

$$\nu^+ = \frac{\nu_t}{\nu} = \underbrace{\kappa y^+ \left(1 - e^{\left(-\frac{y^{+2}}{A^2}\right)}\right)}_{momentum} = \underbrace{\left|\frac{\frac{1}{Pr}-a}{\frac{1}{Pr_t}-a}\right|^{\frac{1+a}{1+2a}} \left|\frac{\frac{1}{Pr}+a+1}{\frac{1}{Pr_t}+a+1}\right|^{\frac{a}{1+2a}}}_{energy}, \quad (12)$$

where the eddy viscosity on the momentum side (left hand side) is estimated from mixing length theory, and on the energy side (Prandtl number, i.e. thermal conductivity) from Yakhot and Orszag's elegant Renormalization Group Theory of turbulence [13] (right hand side). Han and Reitz further simplified this coarse-grained energy equation to extract an algebraic relation for the turbulent Prandtl number from the equality of Equation 12, producing an analytical formula that further assumes: 1) parabolic behavior w.r.t. y^+; 2) constant laminar Prandtl, $Pr = 0.7$.

We extended this formulation by:

1) assuming a generic laminar Prandtl number, computed in each layer from the definition as $Pr = \mu c_p/\lambda$. Very close to the wall, laminar parameters are dominant, and we want this parameter to be as accurate as possible when multicomponent molecular gas properties are available, as a function of temperature and molar composition $\boldsymbol{X}$ [24]:

$$Pr = Pr(T, \boldsymbol{X}), \quad (13)$$

2) assuming a variable turbulent Prandtl number, found from the equality of Equation 12, employing a Newton-Raphson iterative procedure, as:

$$Pr_t = Pr_t\left(y^+, Pr, Pr_{t,\infty}\right). \quad (14)$$

With this enhanced model, laminar and turbulent Prandtl numbers are computed at every node based on the local thermodynamic and flow state, and the only user-defined parameter is the far-field turbulent Prandtl number, $Pr_{t,\infty}$, which can now match that from the CFD solver's enthalpy diffusion term.

Figure 17 shows that the model mostly affects the temperature field prediction. Here, a matrix of four cases is shown with two variables: first, far-field turbulent Prandtl is either 0.72 (same as laminar) or 0.90; second, laminar properties are estimated from either the standard air model (Pr = 0.7), or from the multicomponent properties of combustion products from stoichiometric air-methane combustion (as in the experiment [21]). The discrepancies indicate that better agreement in this case is obtained with lower Prandtl numbers, i.e., when energy diffusion is more significant than momentum diffusion.

Global performance

Overall performance was measured in terms of cycle-averaged heat flux error versus the experimental thermocouple data of [20]. Results for a meaningful selection of all models tested is reported in Figure 18. Results from two equilibrium laws of the wall (Launder-Spalding [12] and Han-Reitz [8]) are also reported, along with their standard deviation values.

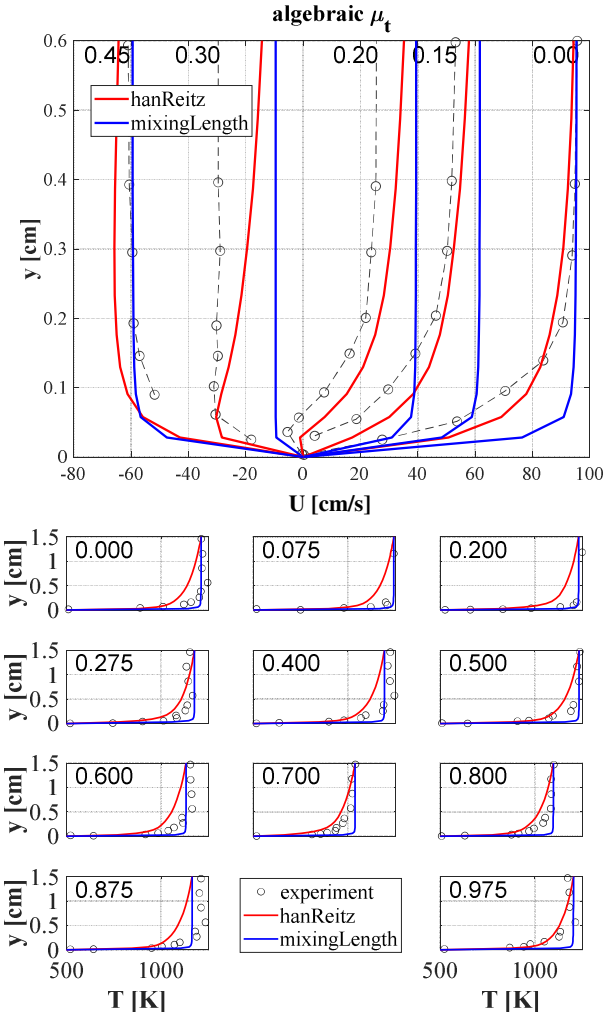

Figure 16. Predicted velocity and temperature profiles according to the algebraic eddy viscosity models. Dashed lines with circle markers are the measured values, while solid lines are the simulation results.

The largest errors were observed from both the equilibrium laws of the wall and the non-equilibrium model with two-equation closure: for both these classes, errors are of order unity, with the well-established Han-Reitz model overestimating the total heat transfer by 84%. This is not the largest error observed overall, as several of the non-equilibrium k-epsilon model predictions exceeded 100% by far (not visualized).

Optimal performance was observed with the non-equilibrium model using the algebraic Han-Reitz eddy viscosity formulation. It is not clear whether its standard form, or the enhanced version presented in this work, will provide the best results in general cases. However, due to the non-equilibrium model, heat flux errors were reduced almost two orders of magnitude down to percent units, with the optimal case (1D model, algebraic, enhanced Prandtl, $Pr_{t,\infty} = 0.72$, multicomponent transport properties) exhibiting only a 1.67% error compared to the experiment.

The standard deviation line shows that all models own non-negligible instantaneous errors; this was in line with the authors of the experiments, who observed non-trivial and unexplained correlation between TLAF temperature at the pipe centerline (shown in Figure

10) and the instantaneous heat probe data, which sometimes have opposite signs.

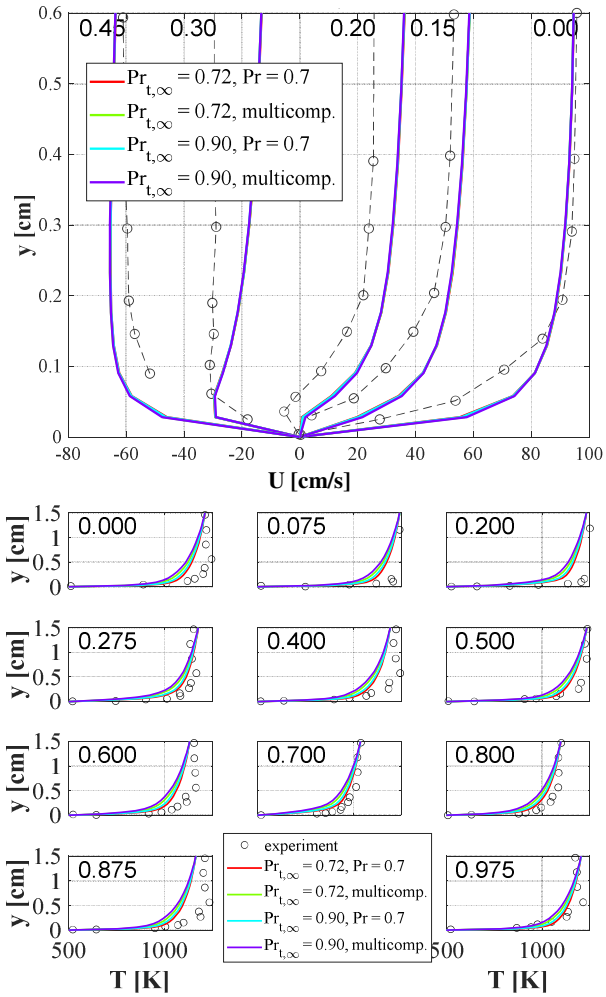

Figure 17. Predicted velocity and temperature profiles according to the algebraic eddy viscosity model with enhanced turbulent Prandtl. Dashed lines with circle markers are the measured values, while solid lines are the simulation results.

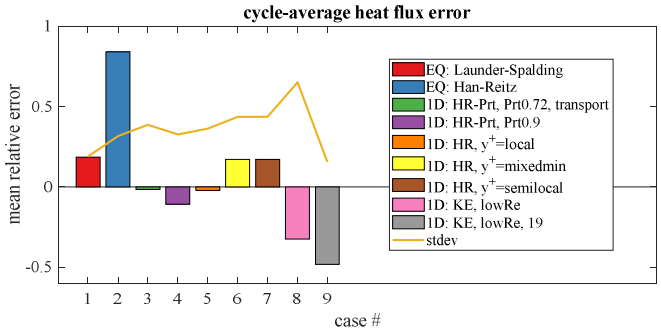

Figure 18. Predicted vs. measured cycle heat flux error for the pulsating combustor case.

Pulsating Flow with axial ∇T

While the non-equilibrium model was exercised standalone for the previous validation, it was then embedded into the FRESCO CFD

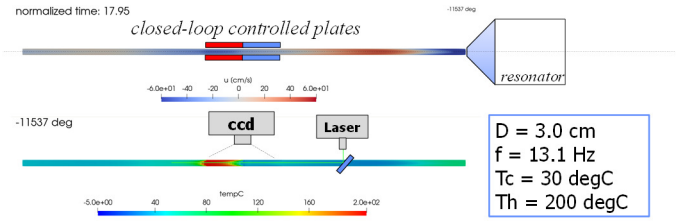

Figure 19. Schematic representing the experimental setup of the 2D pulsatile channel problem.

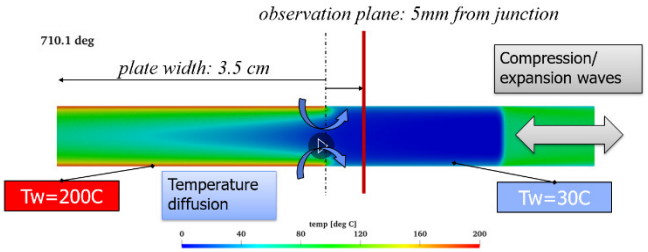

Figure 20. Schematic representing 2D temperature field dynamics in the pulsatile channel problem.

solver [25] as a transient law-of-the-wall model, for validation when coupled with a full CFD solution. The same non-equilibrium wall equations are still solved as an independent 1D problem with proper initial and boundary conditions. While the previous validations relied on experimental (measured) BCs, for the CFD model implementation, they come from the wall face BC (wall side) and from the instantaneous first cell neighbor state on the fluid side of the domain ("far-field" BC).

The experiments of [26] were used for the validation, as represented in Figure 19. These feature a pulsating channel flow case, where flow oscillations are provided by an external resonator (speaker). Far downstream, two closed-loop temperature-controlled plates surround the channel, imposing a step-wise temperature discontinuity from the cold region (T_c=30C) to the hot region (T_h=200C). The pulsatile flow operation featured a Womersley number $Wo = 11$, an oscillation frequency $f = 13.1Hz$, and peak axial velocity U=5.72m/s.

This periodic testcase exhibits a strong two-dimensional wall temperature behavior as shown in Figure 20: at the interface between the two plates, temperature diffusion brings high temperatures back towards the cold side, and inward towards the pipe centerline; overlapped, temperature waves are transported all the way from the resonator through the pipe.

Details of the code's numerics will not be repeated here for the sake of brevity, but they can be found in previous research [27, 14, 28]. Planar Laser Induced Fluorescence (PLIF) temperature measurements were used for the temperature comparisons of Figures 21 to 26, where a selection of equilibrium and transient law-of-the-wall configurations is reported.

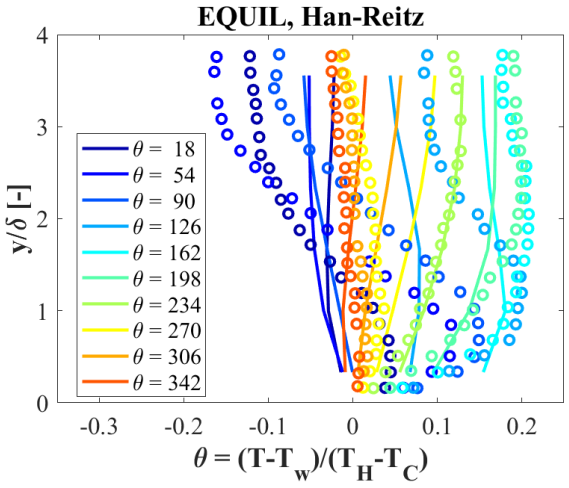

Figure 21. Predicted (solid lines) vs. measured (circle markers) cross-pipe temperatures at several phases. Han-Reitz Equilibrium law of the wall [8].

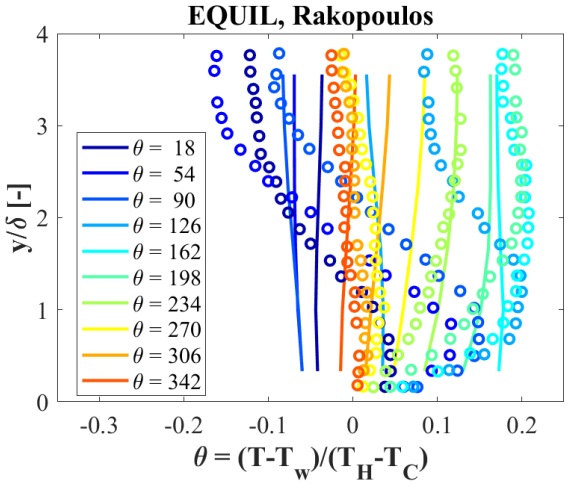

Figure 22. Predicted (solid lines) vs. measured (circle markers) cross-pipe temperatures at several phases. Rakopoulos equilibrium law of the wall [9].

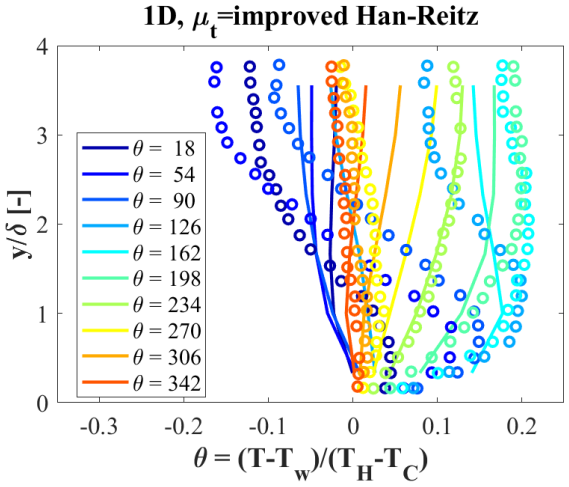

Figure 23. Predicted (solid lines) vs. measured (circle markers) cross-pipe temperatures at several phases. 1D non-equilibrium law-of-the-wall, improved Han-Reitz algebraic viscosity.

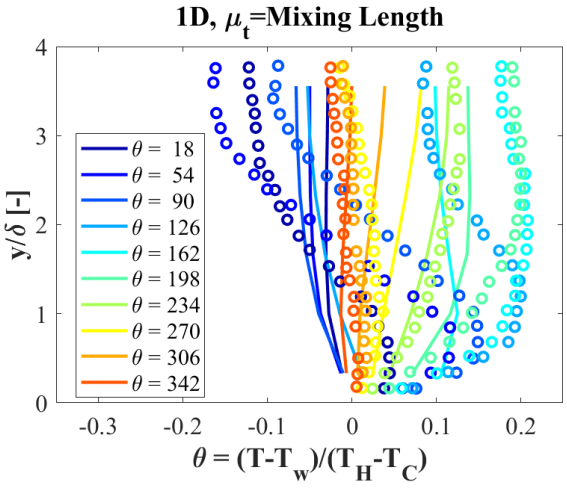

Figure 24. Predicted (solid lines) vs. measured (circle markers) cross-pipe temperatures at several phases. 1D non-equilibrium law-of-the-wall, mixing-length algebraic viscosity.

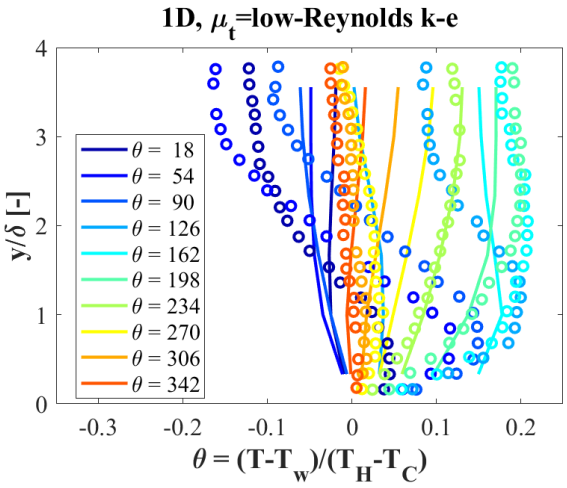

Figure 25. Predicted (solid lines) vs. measured (circle markers) cross-pipe temperatures at several phases. 1D non-equilibrium law-of-the-wall, low-Reynolds k-epsilon turbulence.

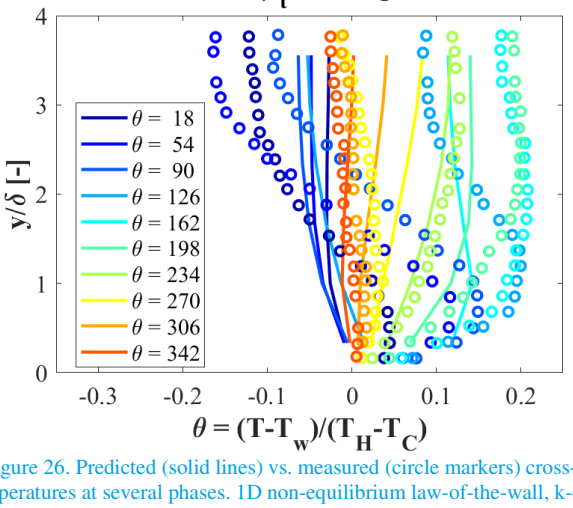

Figure 26. Predicted (solid lines) vs. measured (circle markers) cross-pipe temperatures at several phases. 1D non-equilibrium law-of-the-wall, k-omega turbulence model.

In order to have the 1D law of the wall represent a non-negligible y^+ range, the computational mesh employed 5 cell layers through the pipe's half-size. 50 pulsation cycles were simulated, to allow for the transient flow to be fully established through the pipe. Figures 21 to 26 compare predicted and experimental temperature profiles at a location 5 mm upstream of the plate discontinuity, and at several phases during the cycle.

The following observations were drawn:

- Differences among the boundary layer models are now attenuated by the fact that only the first cell layer close to the wall is being modeled;
- Despite an excellent wall-aligned grid and the problem's low Reynolds number, such differences do exist to a non-negligible extent;
- The Han-Reitz model again has best accuracy, both in its equilibrium (Figure 21) and non-equilibrium (Figure 23) implementations;
- Some equilibrium (Rakopoulos, Figure 22) and non-equilibrium (mixing-length – Figure 24, k-omega – Figure 26) laws of the wall exhibited large deviations from the experiments, even in this relatively simple case;
- All models fail at capturing temperature cooling (blue lines) happening at the early phases due to the pulsation's backward expansion wave.

Because this also happens in all models at the centerline, far from the walls, we think this is due to a turbulence model flaw. K-epsilon models were developed for incompressible cases and they are known to fail at strong-compression flow configurations like jet flows (see [14]); failure of the RNG k-epsilon model to capture the backward cooler expansion wave in the pipe could explain this discrepancy in all cases.

Concluding remarks

A new, one-dimensional, non-equilibrium boundary layer model for momentum and heat transfer predictions in CFD simulations of internal combustion engines was proposed and validated in this work. To assess its performance, experiments were compared against that featured turbulent, compressible, transient flows where local velocity and temperature measurements were available. Model assessment featured:

- Study of the model parameters, most notably: eddy viscosity closure and compressible vs. incompressible formulations;
- Comparison with equilibrium models.

A new algebraic eddy viscosity closure, featuring variable turbulent Prandtl number, was also developed and proposed.

In light of the analysis, the following observations were formulated:

- Improvements in predictive capability over equilibrium models come from having better equations, not from more refined computational discretization: just adding more points was not helpful to achieve correct results, while a good closure for the eddy viscosity was needed.

- Compressibility cannot be neglected in order to capture the correct boundary layer size; a "semi-local" formulation for y^+ with the geometric average of wall and local densities provided the most accurate performance;

- Two-equation turbulence closures do not work well in the boundary layer unless near-wall damping functions are included, which make them similar to an algebraic closure; hence, improved algebraic models are more suitable for the 1D modeling framework;

- With the 1D model, cycle-averaged heat transfer predictions can be accurate within a few percent points relative error, using the proposed variable-turbulent-Prandtl algebraic eddy viscosity when accurate laminar transport properties are available, without any further calibration constants.

The models are being applied to a moving reference frame implementation for internal combustion engine simulations with moving boundaries.

References

[1] L. Fonseca, P. Olmeda, R. Novella and R. Molina Valle, "Internal Combustion Engine Heat Transfer and Wall Temperature Modeling: An Overview," *Archives of Computational Methods in Engineering,* vol. 27, pp. 1661-1679, 2020.

[2] S. Busch, K. Zha, E. Kurtz, A. Warey and R. C. Peterson, "Experimental and Numerical Studies of Bowl Geometry Impacts on Thermal Efficiency in a Light-Duty Diesel Engine," in *SAE Technical Paper 2018-01-0228*, 2018.

[3] S. Busch, K. Zha, F. Perini, R. D. Reitz, E. Kurtz, A. Warey and R. Peterson, "Bowl Geometry Effects on Turbulent Flow Structure in a Direct Injection Diesel Engine," in *SAE Technical Paper 2018-01-1794*, Heidelberg, Germany, 2018.

[4] U. Piomelli and E. Balaras, "Wall-Layer Models for Large-Eddy Simulations," *Annu. Rev. Fluid Mech.,* vol. 34, pp. 349-374, 2002.

[5] R. P. Hessel, R. D. Reitz, A. Srna and R. Rajasegar, "Gaining a better understanding of the mechanics of diesel engine heat transfer when DI-injection schedule changes," in *DoE Advanced Engine Combustion Program Review Meeting*, virtual, 2021.

[6] D. J. Torres and M. F. Trujillo, "KIVA-4: An unstructured ALE code for compressible gas flow with sprays," *Journal of Computational Physics,* vol. 219, no. 2, pp. 943-975, 2006.

[7] B. E. Launder and B. I. Sharma, "Application of the energy-dissipation model of turbulence to the calculation of flow near a spinning disc," *Letters in Heat and Mass Transfer,* vol. 1, no. 2, pp. 131-137, 1974.

[8] Z. Han and R. D. Reitz, "A temperature wall function formulation for variable-density turbulent flows with

application to engine convective heat transfer modeling," *Int. J. Heat Mass Transfer,* vol. 40, no. 3, pp. 613-625, 1997.

[9] C. D. Rakopoulos, G. M. Kosmadakis and E. G. Pariotis, "Critical evaluation of current heat transfer models used in CFD in-cylinder engine simulations and establishment of a comprehensive wall-function formulation," *Applied Energy,* vol. 87, no. 5, pp. 1612-1630, 2010.

[10] P. C. Ma, M. Greene, V. Sick and M. Ihme, "Non-equilibrium wall-modeling for internal combustion engine simulations with wall heat transfer," *International Journal of Engine Research,* vol. 18, no. 1-2, pp. 15-25, 2017.

[11] A. A. Amsden, P. J. O'Rourke and T. D. Butler, "KIVA-II: A computer program for chemically reactive flows with sprays," Los Alamos National Lab, Los Alamos, NM, 1989.

[12] B. E. Launder and D. B. Spalding, "The Numerical Computation of Turbulent Flows," *Numerical Prediction of Flow, Heat Transfer, Turbulence and Combustion,* pp. 96-116, 1983.

[13] V. Yakhot and S. A. Orszag, "Renormalization group analysis of turbulence. I. Basic theory," *Journal of Scientific Computing,* vol. 1, no. 1, pp. 3-51, 1986.

[14] F. Perini, S. Busch, K. Zha and R. D. Reitz, "Comparison of Linear, Non-linear and Generalized RNG-based k-epsilon models for turbulent diesel engine flows," in *SAE Technical Paper 2017-01-0561*, Detroit, MI, 2017.

[15] M. M. Rahman, L. V. Ming and Z. Zhu, "Impact of Prandtl numbers on turbulence modeling," *IOP Conf. Series: Journal of Physics,* vol. 1324, p. 012060, 2019.

[16] D. C. Wilcox, Turbulence Modeling for CFD - Third Edition, San Diego: DCW Industries, 2006.

[17] P. Bradshaw, "Possible origin of Prandtl's mixing-length theory," *Nature,* vol. 249, pp. 135-136, 1974.

[18] A. C. Hindmarsh and K. Radhakrishnan, "Description and Use of LSODE, the Livermore Solver for Ordinary Differential Equations," Lawrence Livermore National Laboratory, Livermore, CA, 1993.

[19] J. H. VanSant, "Conduction heat transfer solutions," Lawrence Livermore National Laboratory UCRL-52863, Livermore, CA, 1980.

[20] J. E. Dec and J. O. Keller, "Time-Resolved Gas Temperatures in the Oscillating Turbulent Flow of a Pulse Combustor Tail Pipe," *Combustion and Flame,* vol. 80, pp. 358-370, 1990.

[21] J. E. Dec, J. O. Keller and I. Hongo, "Time-Resolved Velocities and Turbulence in the Oscillating Flow of a Pulse Combustor Tail Pipe," *Combustion and Flame,* vol. 83, pp. 271-292, 1991.

[22] P. S. Iyer and M. R. Malik, "Analysis of the equilibrium wall model for high-speed turbulent flows," *Phys. Rev. Fluids,* vol. 4, p. 074604, 2019.

[23] N. N. Mansour, J. Kim and P. Moin, "Near-Wall k-epsilon Turbulence Modeling," *AIAA Journal,* vol. 27, no. 8, p. 1068, 1989.

[24] R. J. Kee, M. E. Coltrin and P. Glarborg, Chemically Reacting Flow: Theory & Practive, John Wiley and Sons, Inc., 2018.

[25] F. Perini and R. D. Reitz, "FRESCO - an object-oriented, parallel platform for internal combustion engine simulations," in *28th International Multidimensional Engine Modeling User's Group Meeting at the SAE Congress*, Detroit, 2018.

[26] Z. Yu, X. Mao and A. J. Jaworski, "Heat transfer in an oscillatory gas flow inside a parallel-plate channel with imposed axial temperature gradient," *International Journal of Heat and Mass Transfer,* vol. 77, pp. 1023-1032, 2014.

[27] F. Perini, R. D. Reitz and P. C. Miles, "A comprehensive modeling study of in-cylinder fluid flows in a high-swirl, light-duty optical diesel engine," *Computers and Fluids,* vol. 105, pp. 113-124, 2014.

[28] F. Perini, K. Zha, S. Busch, E. Kurtz, R. C. Peterson, A. Warey and R. D. Reitz, "Piston geometry effects in a light-duty, swirl-supported diesel engine: flow structure characterization," *International Journal of Engine Research,* vol. 19, no. 10, pp. 1079-1098, 2018.

Contact Information

Federico Perini
Federico.Perini@w-erc.com

Acknowledgments

The authors gratefully acknowledge Stanford's prof. Matthias Ihme for the useful discussions.

This work was performed under Sandia Subcontract 1890589, 1, sponsored by the United States Department of Energy, Office of Vehicle Technologies, with program managers Gurpreet Singh and Michael Weismiller, whose financial support is acknowledged.

Sandia National Laboratories is a multi-mission laboratory managed and operated by National Technology and Engineering Solutions of Sandia, LLC., a wholly owned subsidiary of Honeywell International, Inc., for the U.S. Department of Energy's National Nuclear Security Administration under contract DE-NA-0003525. The views expressed in the article do not necessarily represent the views of the U.S. Department of Energy or the United States Government.